Available online at www.sciencedirect.com

jmr&t Journal of Materials Research and Technology

journal homepage: www.elsevier.com/locate/jmrt

Original Article

# Effect of temperature on particle shape, size, and polycrystallinity of Nd-Fe-B powders obtained by hydrogen decrepitation

B.L. Checa Fernández [a,b,*], J.M. Martín [a,b], G. Sarriegui [a,b], N. Burgos [a,b]

[a] CEIT-Basque Research and Technology Alliance (BRTA), Manuel Lardizabal 15, 20018 Donostia / San Sebastián, Spain

[b] Universidad de Navarra, Tecnun, Manuel Lardizabal 13, 20018 Donostia / San Sebastián, Spain

ARTICLE INFO

*Article history:*
Received 5 January 2023
Accepted 11 March 2023
Available online 17 March 2023

*Keywords:*
Nd-Fe-B powder
Hydrogen decrepitation
Particle size
Particle shape
Intergranular fracture
Transgranular fracture

ABSTRACT

This work presents a detailed study of hydrogen decrepitation (HD) to obtain monocrystalline Nd-Fe-B powder. The effect of decrepitation temperature has been investigated to optimize both particle size and shape. Differential scanning calorimetry was applied to analyze the hydrogenation kinetics of $Nd_2Fe_{14}B$ and Nd-rich phases in the range of 25 to 300 °C. Thermogravimetry and X-ray diffraction allowed determining the hydrogen absorption of the whole alloy and the matrix phase, respectively. While scanning electron microscopy (SEM) was used to visualize particle shape and size, dynamic image analysis was applied to evaluate quantitatively these properties. The high monocrystallinity of the powder was confirmed by electron backscattering diffraction. The partial pressure of hydrogen required to initiate the hydrogenation reactions decreases when the temperature increases. The hydrogen absorbed by the whole alloy and, in particular, by the $Nd_2Fe_{14}B$ phase decreases with temperature. Below 150 °C, the hydrogen absorbed by the $Nd_2Fe_{14}B$ phase produces a significant transgranular cracking that is undesirable for particle shape. At 300 °C, the fast and limited absorption of hydrogen by the Nd-rich phase causes insufficient intergranular fracture and, hence, polycrystallinity. Between 150 and 300 °C, the controlled fragmentation resulted in monocrystalline particles with a more equiaxial shape, which is a suitable precursor to develop anisotropic ultrafine powders by the hydrogenation, disproportionation, desorption, recombination (HDDR) process.

© 2023 The Authors. Published by Elsevier B.V. This is an open access article under the CC BY license (http://creativecommons.org/licenses/by/4.0/).

## 1. Introduction

Permanent magnets are essential components in many fields of technology because of their ability to provide a strong magnetic flux, avoiding the need for any external energy supply. The magnetic Nd-Fe-B alloys have steadily grown in relevance since the first permanent magnets were manufactured with this material in 1984 [1,2]. The high remanence and coercivity of this material are due to the intrinsic properties of

* Corresponding author.
E-mail address: bcheca@ceit.es (B.L. Checa Fernández).

https://doi.org/10.1016/j.jmrt.2023.03.076

2238-7854/© 2023 The Authors. Published by Elsevier B.V. This is an open access article under the CC BY license (http://creativecommons.org/licenses/by/4.0/).

the $Nd_2Fe_{14}B$ compound and the specific microstructural features developed during processing. The microstructure normally contains two other phases: Nd-rich phase at grain boundaries and a minor fraction of $NdFe_4B_4$ phase [3]. The so-called Nd-rich phase is composed of several metallic and oxide compounds [4–6], as the double hexagonal close-packed Nd (dhcp-Nd), the face-centered cubic NdOx (fcc-NdOx) or the hexagonal closed packed $Nd_2O_3$ (hcp-$Nd_2O_3$) [7,8].

Previous studies have shown that gas atomization can indeed be used as a viable alternative for mass production of Nd-Fe-B alloy powder [9–11]. The particle size distribution can be adjusted in a wide range by a proper selection of process parameters [12–15], maximizing the yield for any specific subsequent processing. Other favorable characteristics of gas atomized powders are the spherical shape [16,17] and the low oxygen content. The typical microstructure of gas atomized powder contains $Nd_2Fe_{14}B$ isotropic grains of approximately 5 μm, which limits the maximum remanence achieved in the magnet [11].

The hydrogenation, disproportionation, desorption, recombination (HDDR) process is used to refine micrometric $Nd_2Fe_{14}B$ grains down to 300 nm [18]. Moreover, if the process is properly controlled, the recombined grains inherit the crystallographic texture of the prior grain [19–21]. The increase in the demand of anisotropic Nd-Fe-B powder for the manufacture of bonded magnets makes the HDDR process an interesting technique to transform scrap of sintered Nd-Fe-B magnets into anisotropic powders [22–24]. Theoretically, if grain growth is induced by annealing in a gas atomized powder until the particles become monocrystalline, the HDDR process could be applied subsequently to produce an ultrafine anisotropic powder. This HDDR powder could be an interesting material for the preparation of anisotropic bonded magnets [25]. Previous results have demonstrated that the temperature to induce grain growth in polycrystalline gas atomized particles is so high that the particles form a sintered block [11]. Consequently, hydrogen decrepitation (HD) has to be applied to transform the annealed material into loose powder before the HDDR process. This new process has been carried out in a previous European project (https://neohire.es/), using a ternary Nd-Fe-B gas atomized powder without the requirement for additional heavy rare earth or critical raw materials, obtaining an anisotropic powder.

The HD process was first patented in 1979 [26] as a new method to break down $SmCo_5$ and $Sm_2(Co,Fe,Cu,Zr)_{17}$ ingots into powder. Subsequently, this process was applied to the newly developed Nd-Fe-B alloy with the same purpose [27]. HD is a mandatory step in the manufacturing and recycling of modern Nd-Fe-B magnets [22]. This process is based on the formation of neodymium (and other rare earths) hydrides through the reaction of the material with a hydrogen atmosphere. Two different sequences of reactions take place. Firstly, the Nd-rich phase reacts with the hydrogen to form its hydride as follows:

$$Nd + H_2 \rightarrow NdH_2 \quad \text{(Ec. 1)}$$

$$NdH_2 + x/2H_2 \rightarrow NdH_{2+x} \quad \text{(Ec. 2)}$$

This is an exothermic reaction that activates the second stage, in which the matrix phase is hydrogenated. Here, hydrogen atoms penetrate through pores, microcracks and by diffusion to occupy interstitial sites in the $Nd_2Fe_{14}B$ crystal lattice [28]:

$$Nd_2Fe_{14}B + y/2H_2 \rightarrow Nd_2Fe_{14}BH_y \quad \text{(Ec. 3)}$$

where $0 \leq y \leq 5.5$. The hydrogenation of the ferromagnetic $Nd_2Fe_{14}B$ phase reduces its anisotropy field ($H_A$) from 70.7 kOe (5626 kA/m) to 17.5 kOe (1393 kA/m), leading to a low coercivity value and a reduction of the maximum energy product $(BH)_{max}$. Hydrogenation also influences the Curie temperature ($T_c$) via exchange interactions.

During the hydrogenation process, a volume expansion takes place, which promotes the formation of transgranular and intergranular cracks, causing the breakup of the material [29]. Fig. 1 shows the different types of fracture that can occur during the hydrogen decrepitation process. The hydrogenation of the grain boundary phase can lead to an increase in its volume of up to 16% [30]. This volumetric expansion causes stresses that promote crack propagation mainly along grain boundaries. In addition, the unit cell of the matrix phase expands between 4 and 6%, because the interstitial sites, such as 8j, 16k, and 4e, are occupied by the hydrogen atoms [31]. As the main expansion is due to the Nd-rich phase, the dominant fracture mode is intergranular cracking. Nevertheless, transgranular cracking also takes place to some extent (Fig. 1b). The HD powders are very friable because of the presence of microcracks in the particles [32]. It is better to maximize intergranular cracking (Fig. 1c), since it results into particles that are more equiaxial and flow better during the subsequent shaping of the bonded magnet. Additionally, if intergranular crack propagation does not take place along all the grain boundary phase, some of the resulting particles will contain two or more grains, reducing the anisotropy degree of the obtained powder (Fig. 1d).

The amount and rate of hydrogen absorption, as well as of heat release, depend on the temperature and hydrogen pressure. These variables affect the fracture mode. A recent study [33] determined that the amount of cracks formed in the $Nd_2Fe_{14}B$ phase can be controlled by changing the temperature during the hydrogen decrepitation process. Moreover, it was demonstrated that the reduction of the number of intragranular cracks led to an anisotropy improvement after the HDDR process. The improvement in the magnetic properties was due to the increase in the fraction of laminar microstructure formed during the disproportionation process, leading to highly aligned $Nd_2Fe_{14}B$ grains after recombination.

In general, the diffusion of hydrogen in metals is extremely rapid. In some cases, diffusivities can reach values in the order of $10^{-4}$ $cm^2s^{-1}$ [34]. Diffusivities follow the Arrhenius law:

$$D = D_0 \exp(-E_a / k_T) \quad \text{(Ec. 4)}$$

where D is the diffusivity, $D_0$ the preexponential factor, $E_a$ the activation energy, k the Boltzman's constant, and T the absolute temperature. Thus, diffusion increases exponentially with temperature. These high diffusion rates are associated with low activation energy values. Moreover, surface effects play a significant role in the hydrogen adsorption by Nd-Fe-B alloys, which is a necessary previous step to the diffusion of hydrogen atoms into the bulk. The increase of the specific

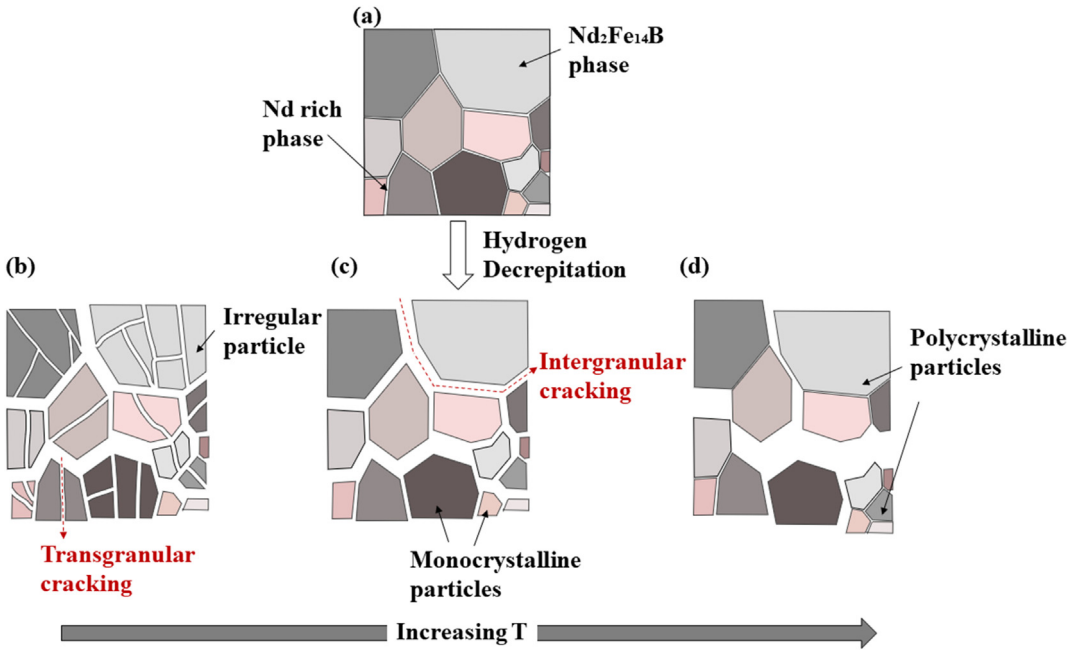


**Fig. 1 – Schematic representation of the different fracture types that can occur during hydrogen decrepitation: (a) initial annealed sample, (b) intergranular and transgranular cracking, (c) complete intergranular cracking and (d) insufficient intergranular cracking.**

surface due to the decrepitation of the sample has a considerable impact on the progress of the hydrogen diffusion, accelerating the process by five orders of magnitude in comparison with the bulk sample [35].

The success of a bonding process of HDDR powders depends on the size and shape of the particles because it will influence the flowability of the feedstock. For that reason, HD particles must possess the optimal particle size distribution (PSD) and shape. Although the decrepitation process of this material has been previously reported in the literature, there are not publications that focus on the optimization of particle size and shape of these powders. Moreover, we also propose a systematic study of the particle size and shape conducted by dynamic image analysis, providing relevant information on the relationship between these properties and the decrepitation temperature, which has not yet been reported in the literature. The objective of this research is to optimize the HD process variables to obtain a monocrystalline Nd-Fe-B powder after annealing for grain growth an isotropic polycrystalline gas atomized powder, which can constitute a new technique for the production of anisotropic powder for the manufacture of bonded magnets.

## 2. Experimental procedure

The Nd-Fe-B powder was produced by gas atomization with Ar in a PSI model HERMIGA 75/3VI unit using a convergent-divergent close-coupled atomizer, used in recent atomization studies [36]. Before the atomization, the chamber was evacuated (up to 0.1 mbar) and purged with Ar several times to minimize oxidation. The raw materials were induction melted and alloyed in a high purity alumina crucible. This system can produce up to 3 kg of powder per batch.

Before conducting the grain growth annealing, particles larger than 150 μm were removed by sieving because this fraction contained a significant number of splats (flake-like particles formed when melt droplets hit the walls of the atomization chamber before they have solidified). The heat treatment was carried out in an alumina crucible at 1100 °C for 96 h under Ar using the size fraction <150 μm. These conditions were chosen based on previous results of the group [11].

The heat treatment resulted in the formation of a sintered block, so HD was researched as a way of obtaining a monocrystalline powder. Simultaneous differential scanning calorimetry (DSC) and thermogravimetry (TGA) were used to analyze the hydrogenation kinetics of $Nd_2Fe_{14}B$ and Nd-rich phases, since these reactions are strongly exothermic. Experiments were conducted in a calorimeter SETARAM model SETSYS EVOLUTION 16–18 using a sample of about 100 mg. Firstly, the chamber was heated under vacuum (~$10^{-2}$ mbar) to the desired temperature (25, 50, 100, 150 or 300 °C). Next, hydrogen was introduced at a constant flow rate of 16.16 ml/min, increasing progressively the pressure in the chamber up to 1100 mbar, which was reached in about 2 h. Moreover, a sample of 10 g was decrepitated in a furnace under 1 bar of hydrogen at different temperatures for 6 h, to measure the particle size distribution and shape parameters. The weight fraction of equilibrium phases as a function of temperature for the Nd-Fe-B composition has been calculated using the software Thermo-Calc version 2020b using the database SGTE Solutions Database (SSOL) version 4.9.

The particle size distribution of as-atomized and HD powders was measured by dynamic image analysis in an

**Table 1 – Chemical composition of the atomized powder.**

| Prop. | Concentration (wt.%) | | | | | | | | | | |
|---|---|---|---|---|---|---|---|---|---|---|---|
| | Nd | Fe | B | Co | Si | Cr | Sm | O | N | C | S |
| Mean | 30.93 | 67.92 | 1.087 | <0.00497 | 0.0170 | 0.0048 | 0.145 | 0.044 | 0.0019 | 0.0183 | 0.00081 |
| St. dev. | 0.02 | 0.05 | 0.005 | 0.00007 | 0.0007 | 0.0001 | 0.003 | 0.001 | 0.0002 | 0.0003 | 0.00005 |

equipment SYMPATEC QICPIC VIBRI/L. This image processing technique has been previously used to quantitatively evaluate the particle shape and distribution of superalloy powders [37]. The particle size is reported as the diameter of a circle of equal projection area. Aspect ratio is defined as the ratio of the minimum to the maximum Feret diameter, so that it is always a number comprised between 0 and 1. It measures the elongation of the particle, i.e. when the aspect ratio increases, the corresponding particle is more equiaxial (or less elongated) and, as a result, less irregular.

The chemical composition of the powders was measured by inductively coupled plasma-optical emission spectrometry (ICP-OES) in an instrument VARIAN model 725-ES. The oxygen and nitrogen concentrations were measured with an analyzer LECO model TC-400, and the carbon and sulfur with a LECO model CS-200. The hydrogen content was measured with an instrument LECO model OHN836. The constituent phases and the lattice parameters were studied by X-ray diffraction (XRD) with a diffractometer BRUKER model D8 ADVANCE. XRD patterns were analyzed with the software TOPAS V6.0. Scanning electron microscopy (SEM) was used to observe the particle shape and the microstructure in a high-resolution instrument JEOL model JMS 7100F.

For microstructural observation and electron backscattered diffraction (EBSD) analysis, the sample was mounted in an epoxy resin and cured at room temperature. Next, the sample was ground with SiC abrasive papers and then polished with several diamond suspensions, reducing progressively the abrasive particle size. The last polishing step was carried out with a suspension of $SiO_2$ (abrasive particle size of 0.04 μm).

Grain size was measured following well established quantitative metallographic procedures. Due to the high Nd content of the studied sample (30.93 wt%) grain boundaries can be easily revealed by etching. The annealed sample has been etched with Vilella's reagent (1 g of picric acid, 5 ml of

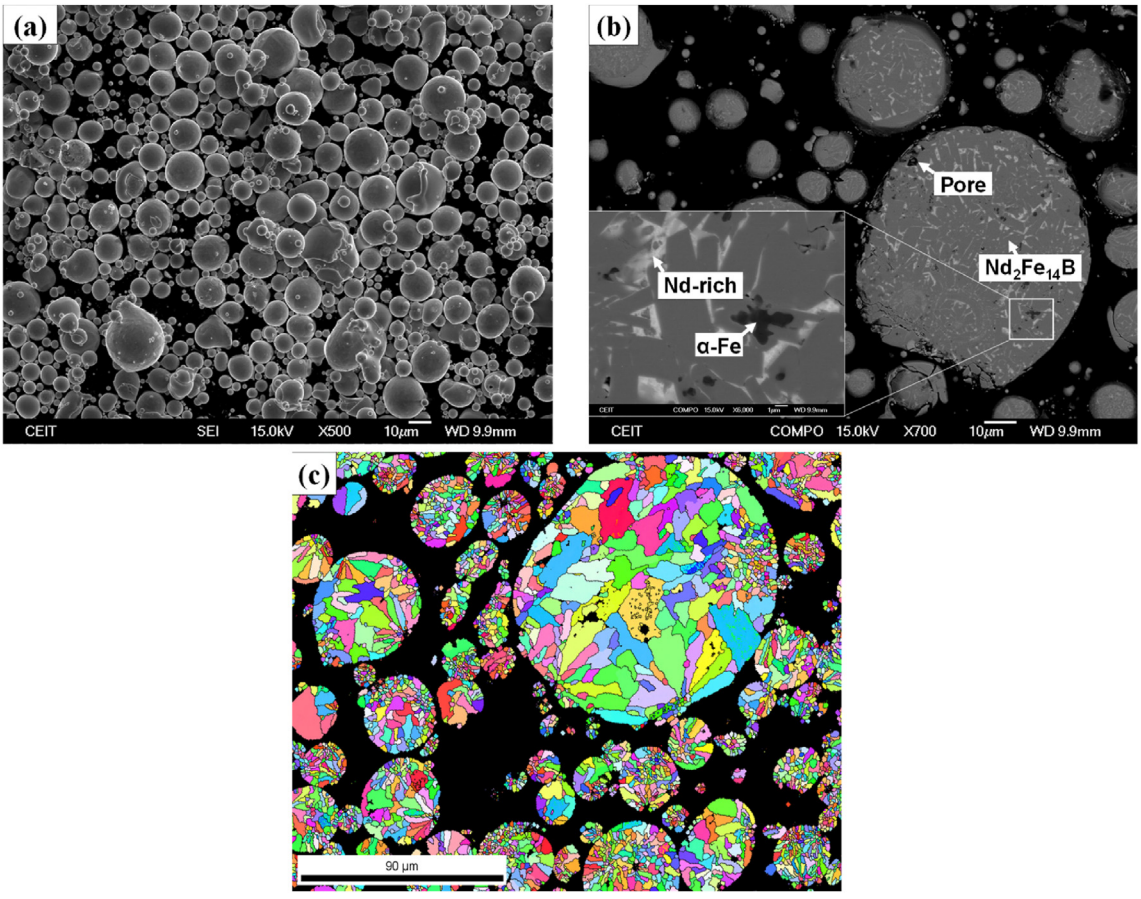


**Fig. 2 – SEM images of the as-atomized powder, powder fraction <150 μm: (a) particle shape, (b) microstructure, and (c) inverse pole figure (IPF).**

HCl, and 100 ml of ethanol) for 10 s, cleaned, and dried. The microstructural images used for the quantification of the grain size distribution were taken in an optical microscope (LEICA model DMI 5000 M). Each picture was digitalized using the image analysis software LEICA APPLICATION SUITE software (LAS v4.5.0). The same program was applied to quantify the grain size, measuring more than 600 different grains. The grain size is reported as the arithmetic mean of the statistical distribution of equivalent diameters. The equivalent diameter is defined as the diameter of the cross-sectioned circle with the same area as the grain. The mean grain size is reported along with a 95% confidence interval.

EBSD was utilized for analyzing the polycrystallinity of grains and particles. A field emission gun scanning electron microscope (JEOL JSM-7100F) equipped with an OXFORD Symmetry S3 detector and the Aztec 5.0 SP1 software was used to collect and index the Kikuchi patterns. The EBSD mappings were performed using an accelerating voltage of 30 kV and a scan step of 0.5 μm. The scans were analyzed and cleaned using the TSL OIM™ Analysis 5.31 software. The cleaning method consisted on a grain dilatation step based on a single iteration. The minimum grain size to apply the clean-up procedure was 3 pixels surrounded by a boundary (grain tolerance angle) of >15° in misalignment.

## 3. Results and discussion

### 3.1. Powder characterization

For this study, a 31.5Nd-bal.Fe-1.1B (wt.%) ternary alloy has been used. Table 1 displays the true composition of the produced powder. As can be seen, the atomized powder presents a chemical composition very close to the nominal one, showing good control of the chemistry during melting and alloying. Additionally, the powder has a low oxygen content of 440 ppm. Such a low level is quite difficult to achieve when highly reactive elements (i.e. Nd) are in the composition of the alloy [38].

Fig. 2 shows representative SEM images illustrating the particle shape and microstructure of as-atomized powder after removing particles >150 μm due to the presence of splats. As expected for an inert gas atomization process [39], particles are spherical. The microstructure consists of a solidification structure with two main phases, $Nd_2Fe_{14}B$ (light grey) and Nd-rich phase (white). Some α-Fe (dark grey) has also been detected. The amount of this soft magnetic, metastable phase is low, since cooling rates in atomization are high and the alloy contains a high concentration of Nd. It has been noticed that α-Fe is present more frequently in large particles than in

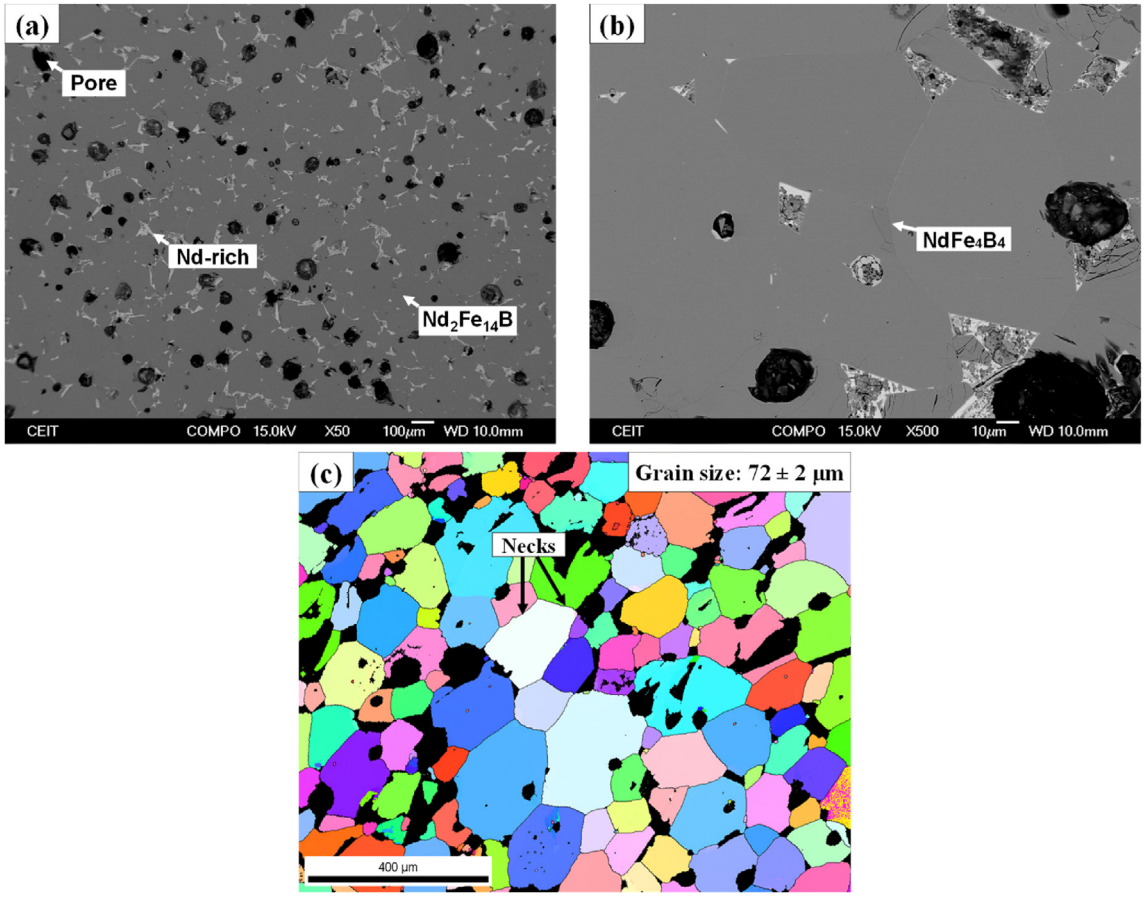


**Fig. 3 – Microstructure of grain growth annealed powder: (a) backscattered electron image at low magnification, (b) backscattered electron image at high magnification, and (c) IPF image.**

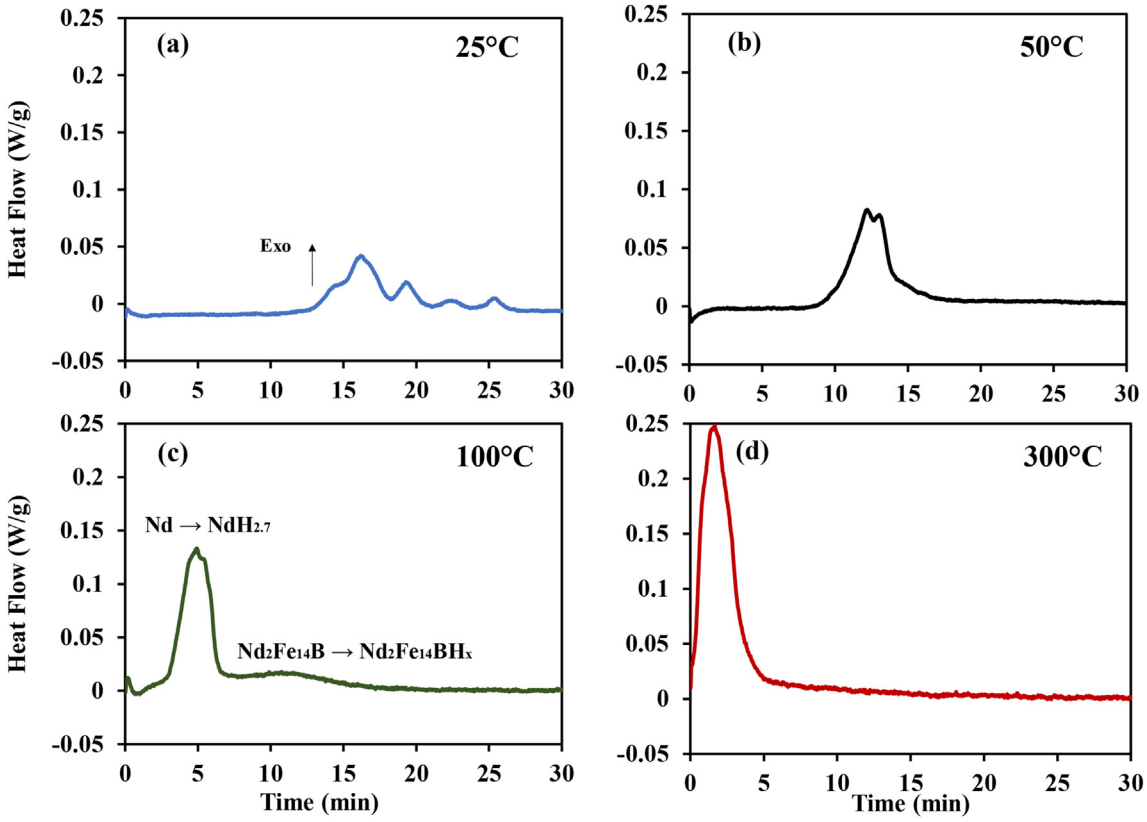


**Fig. 4 – Effect of temperature on heat flow during hydrogen decrepitation: (a) 25, (b) 50, (c) 100, and (d) 300 °C.**

the small ones due to the difference in cooling rate. Some internal porosity (black) was also observed. Fig. 2c shows the inverse pole figure (IPF) of as-atomized powder. It can be remarked that bigger particles have bigger grain size, due to the lower cooling rate during the atomization process. The particles are polycrystalline with an average grain size <10 μm, so the application of the HDDR process to this material would be effective in reducing the grain size and improving the coercivity, but the resulting powder would be isotropic. A grain growth annealing process followed by HD was implemented to obtain an anisotropic monocrystalline powder.

### 3.2. *Annealing*

Fig. 3 shows the microstructure of the powder after annealing. The main phases observed in Fig. 3a are $Nd_2Fe_{14}B$ (light grey) and Nd-rich phase (white). The metastable α-Fe has disappeared. Fig. 3b shows a minor formation of the $NdFe_4B_4$ phase. The IPF image of Fig. 3c demonstrates that the annealing has been successful to promote grain growth, since grain size has increased from <10 μm to 72 ± 2 μm. Unfortunately, necks have also developed within the particles by liquid phase sintering, forming a block. The pictures also display large intergranular pores (black). The oxygen content of the annealed sample is 0.0740 ± 0.0008 wt%, showing a low increase during this heat treatment.

### 3.3. *Hydrogen decrepitation (HD)*

Fig. 4 shows the isothermal heat flow traces measured as a function of time at different temperatures. The traces exhibit different exothermic peaks, associated with the hydrogenation of the sample. The first peak is linked with the

**Table 2 – Parameters and hydrogen content obtained for the HD reaction of the annealed sample at different temperatures.**

| T (°C) | $\Delta m/m_o$ (%) | ΔH (J/g) | $t_o$ (min) | $t_f$ (min) | Reaction length ($t_f$-$t_o$) (min) | Hydrogen content (ppm) |
|---|---|---|---|---|---|---|
| 25 | 0.51 | −13.44 | 10 | 29 | 19 | 3600 ± 100 |
| 50 | – | −15.99 | 8 | 23 | 15 | 3570 ± 80 |
| 100 | 0.41 | −27.59 | 6 | 19 | 16 | 3290 ± 60 |
| 150 | 0.38 | −28.37 | 1 | 12 | 11 | 3000 ± 100 |
| 300 | 0.00 | −29.28 | 0 | 6 | 6 | 1840 ± 90 |

Symbols: T: temperature; $\Delta m/m_o$: mass gain; ΔH: enthalpy change; $t_o$: initial reaction time; $t_f$: end reaction time.

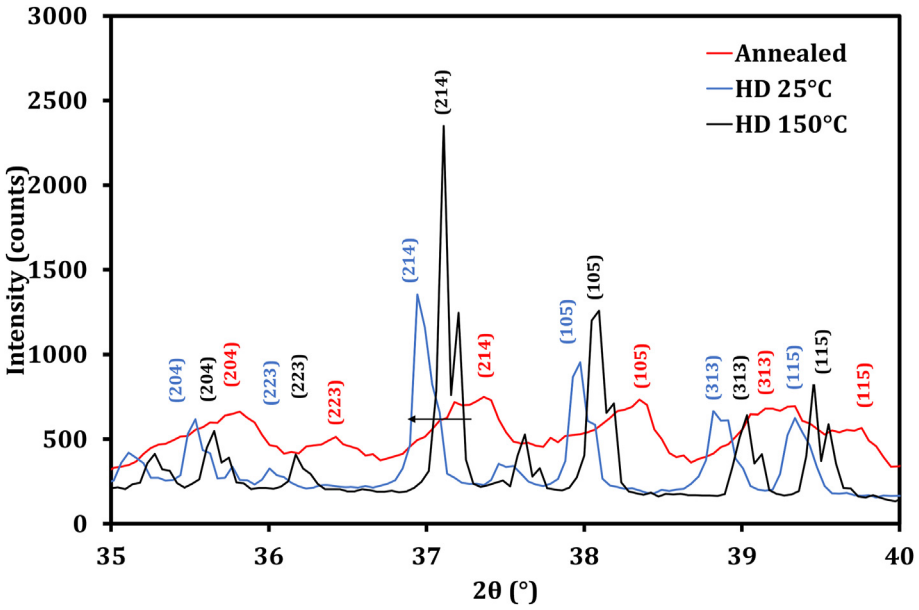


**Fig. 5 – XRD patterns of the annealed sample and the powders after HD at 25 and 150 °C.**

hydrogenation of the Nd-rich phase, while subsequent peaks are caused by the activation and hydrogenation of the matrix phase $Nd_2Fe_{14}B$. At 25 °C, the hydrogenation of the $Nd_2Fe_{14}B$ phase occurs in several steps and at a slow rate. Only one peak corresponding to the formation of $Nd_2Fe_{14}BH_y$ is observed between 50 and 150 °C, and the reaction ends at a shorter time. Moreover, this peak disappears at 300 °C, which means that no noticeable hydrogenation of the matrix phase has taken place or that both reactions occur in such a short time that the two peaks are overlapped.

Table 2 displays the times for the beginning and end of the reactions, as well as the reaction length. The acceleration of hydrogenation kinetics is noticeable with the rise of the temperature. Thus, the total reaction length is reduced from 19 to 6 min when the temperature is raised from 25 to 300 °C. The table also shows that hydrogen absorption ($\Delta m/m_o$) decreases with the temperature, producing a lower volume expansion [40]. Finally, Table 2 shows that the absolute value of the reaction enthalpy increased from 13.44 to 29.28 J/g in the studied temperature range, revealing that the overall process is more exothermic (the negative sign indicates heat release) with temperature.

As mentioned before, the literature reports that the number of hydrogen atoms per unit formula ("y" in equation (3)) absorbed by the matrix during the hydrogenation varies from 1 to 5.5. We have estimated this value for the different hydrogenation temperatures using the measured weight gain and hydrogen content. In order to do the calculation, several simplifications are necessary. Firstly, the weight percentage of the different phases in the alloy under equilibrium conditions has been calculated using the software Thermo-Calc. The calculated weight percentages of phases $Nd_2Fe_{14}B$, Nd-rich phase, and $NdFe_4B_4$ are 92.88%, 5.56%, and 1.56%, respectively. The influence of temperature, in the range from 25 to 300 °C, on these weight fractions is negligible. Based on the experimental evidence found in the literature [41], it is accepted that phase $NdFe_4B_4$ does not hydrogenate in the temperature region below 500 °C. It is well established that the Nd-rich phase is in fact a mix of different compounds whose relative amount depends on the zone and the thickness of the intergranular phase [5]. Moreover, its average elemental composition contains significant amounts of Fe, B, and O, along with Nd [42]. In order to estimate the hydrogen absorbed by this complex phase, it will be considered that it hydrogenates as Nd does, i.e. it contains the same hydrogen per unit mass as $NdH_{2.7}$. Additionally, the experimental evidence indicates that the Nd-rich phase does not release hydrogen until it is heated above 200 °C in vacuum [43]. Consequently, it will be assumed that the Nd-rich phase is fully hydrogenated in the range of temperatures studied by this method (25-150 °C) under hydrogen. The error due to these simplifications should be small, since the weight fraction of the Nd-rich phase in the alloy is small (5.56 wt%). Accepting these hypotheses, the mass gain of the alloy due to the hydrogenation of the Nd-rich phase has been calculated to be 0.105 wt%.

XRD has been used to measure the lattice parameters of the tetragonal compound $Nd_2Fe_{14}BH_y$. The other phases could not be detected by this technique. During the decrepitation process, hydrogen atoms enter into the crystal lattice of the matrix phase increasing its lattice parameters. As a result, the diffraction peaks of this phase are shifted toward lower Bragg

**Table 3 – Lattice parameters of tetragonal phase $Nd_2Fe_{14}BH_y$ annealed and after HD (25, 100, 150, and 300 °C).**

| Specimen | a (Å) | c (Å) |
|---|---|---|
| Annealed | 8.8353 | 12.2475 |
| HD 25 °C, 6 h | 8.8963 | 12.3206 |
| HD 100 °C, 6 h | 8.8745 | 12.3035 |
| HD 150 °C, 6 h | 8.8676 | 12.2978 |
| HD 300 °C, 6 h | 8.8415 | 12.2480 |

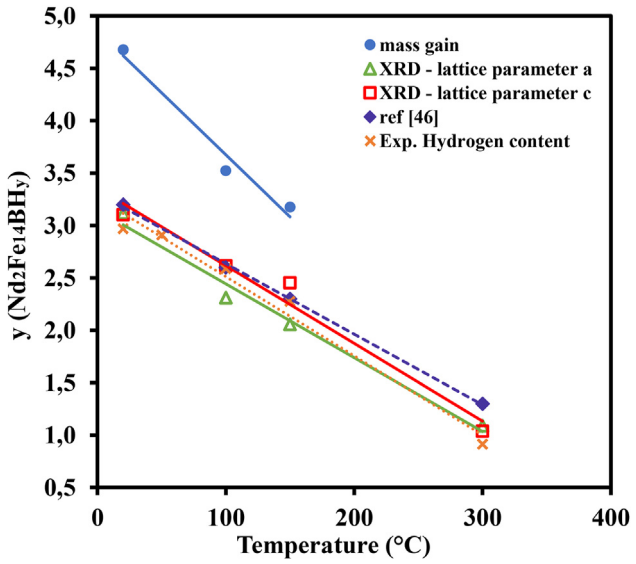


**Fig. 6 – Estimation of hydrogen atoms per unit formula (y) in the hydrogenated matrix phase $Nd_2Fe_{14}BH_y$ in the range 25–300 °C by different methods: (●) mass gain by TGA, (▲) lattice parameter "a", (■) lattice parameter "c", and (x) measured hydrogen content.**

angles, as shown in Fig. 5, where the XRD pattern of the annealed sample is compared with those of the HD samples. Table 3 shows that the lattice parameters of the annealed powder are lower than those of the samples after HD at different temperatures. In the hydrogenated state, Fig. 5 illustrates the shift of the diffraction peaks to higher angles for the powder decrepitated at 150 °C as compared to that decrepitated at 25 °C. Table 3 demonstrates that the lattice parameters go down with increasing hydrogenation temperature, which corroborates the lower hydrogen absorption of

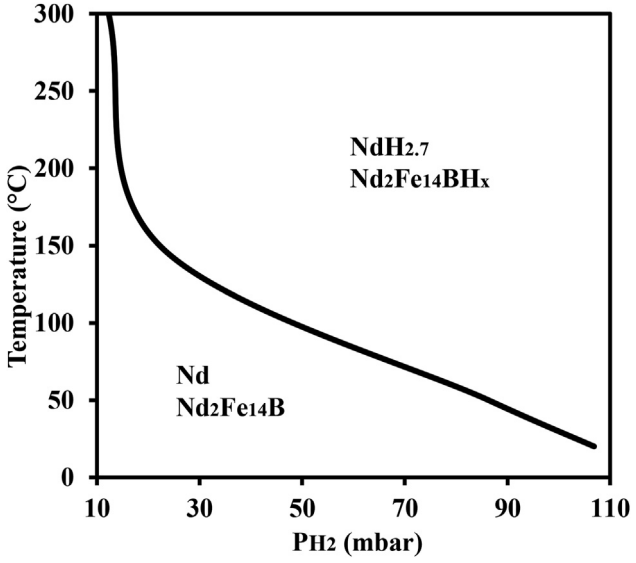


**Fig. 7 – Temperature-hydrogen pressure phase diagram for 31.5Nd-67.4Fe-1.1B (wt.%) alloy.**

the $Nd_2Fe_{14}BH_y$ when the temperature is raised (see Table 2). Reducing the hydrogenation of the matrix phase will decrease the formation of internal microcracks in the particles. These microcracks are known to act as fast diffusion channels for the hydrogen during HDDR, worsening the amount of desirable lamellar microstructure [44,45] and the anisotropy of the final powder [33]. Thus, it is important to minimize the hydrogenation of the matrix phase during HD for the subsequent application of the HDDR process on this powder. The hydrogen atoms absorbed by the matrix phase have been also estimated by comparing the measured lattice parameters with those reported in literature for phase $Nd_2Fe_{14}BH_y$ [31]. The values calculated from both lattice parameters are equivalent in the studied temperature range (25–300 °C).

Fig. 6 compares the hydrogen atoms absorbed per unit formula calculated from XRD data, from mass gain (TGA) and from the measured hydrogen content (Table 2). In all cases, the trend is similar. The number of hydrogen atoms in the matrix phase decreases with the temperature. The results are in the range of the values reported in previous publications. At high temperature (300 °C), the total mass gain of the alloy is so low that the hydrogenation of the matrix phase cannot be estimated by this method. However, the XRD results show that $y = 1.09$ and the measured hydrogen content provides a value of $y = 0.91$. These values are in agreement with a previous research [46] in which they measured the hydrogen content as a function of temperature at a constant pressure of 250 mbar; these values have been included in Fig. 6 for comparison. Consequently, XRD method seems to be more reliable than TGA and allows estimating the hydrogenation degree of the matrix phase over a wider temperature range. Likely, the error of TGA estimations is larger because of a lower sensitivity of the technique.

Since the thermodynamic system contains four elements (impurities are neglected), a complete phase diagram contains five independent axes (three of composition, one of temperature, and another of pressure). In order to represent this space in two dimensions, it is necessary to fix three degrees of freedom. This has been realized by fixing the compositional ratio between B, Nd, and Fe to match the composition 31.5Nd-67.4Fe-1.1B (wt.%), which introduces two restrictions (Nd/B and Fe/B ratios), and by making the total pressure equal to the hydrogen pressure. Notice that, in order to fix the composition of each equilibrium state, it is not enough to know the composition of the non-hydrogenated alloy, since this one is going to absorb different amounts of hydrogen depending on temperature and overall pressure. Thus, the last restriction fix at the same time the composition of the final system and the total pressure. In this way, the equilibrium states can be represented in a diagram with two axes, one for the temperature and another for the pressure. The temperature-hydrogen pressure phase diagram is presented in Fig. 7. The phases $Nd_2Fe_{14}B$ and Nd are stable on the left side of the curve, whereas $Nd_2Fe_{14}BH_y$ and $NdH_{2.7}$ are stable on the right. Here, it is important to highlight that the transitions $Nd_2Fe_{14}B$/$Nd_2Fe_{14}BH_y$ and Nd/$NdH_{2.7}$ should be theoretically marked by two separate lines. However, the experimental results suggest that both lines are very close, so they cannot be actually resolved, i.e. only one line is observed in practice. The diagram

shows that the minimum temperature required to form $Nd_2Fe_{14}BH_y$ and $NdH_{2.7}$ decreases as the hydrogen pressure increases.

Fig. 8 shows the powder after hydrogen decrepitation. As mentioned before, when the temperature is raised, the absorption of hydrogen by the matrix phase is decreased. Consequently, transgranular breakup is reduced, resulting in a larger particle size and a more equiaxial particle shape. For example, at 25 and 50 °C, Fig. 8a and b shows the presence of very irregular particles that are significantly smaller than the grains shown in Fig. 3c (~72 μm); those are the outcome of transgranular cracking. On the other hand, when the temperature is raised, the kinetics of hydrogenation is faster and more heat is released in a shorter time. As a result, at 300 °C (Fig. 8e), it is observed some transgranular cracking (very irregular small particles), but also insufficient intergranular fragmentation. As shown in the heat flow graph of Fig. 4 at 300 °C, the hydrogenation reaction of the Nd-rich phase takes place too fast, which precludes crack propagation along all grain boundaries. This behavior results in some large, polycrystalline particles, as displayed in Fig. 9, where a particle containing two different grains can be observed. The presence of polycrystalline particles will reduce the anisotropy of the final HDDR powder.

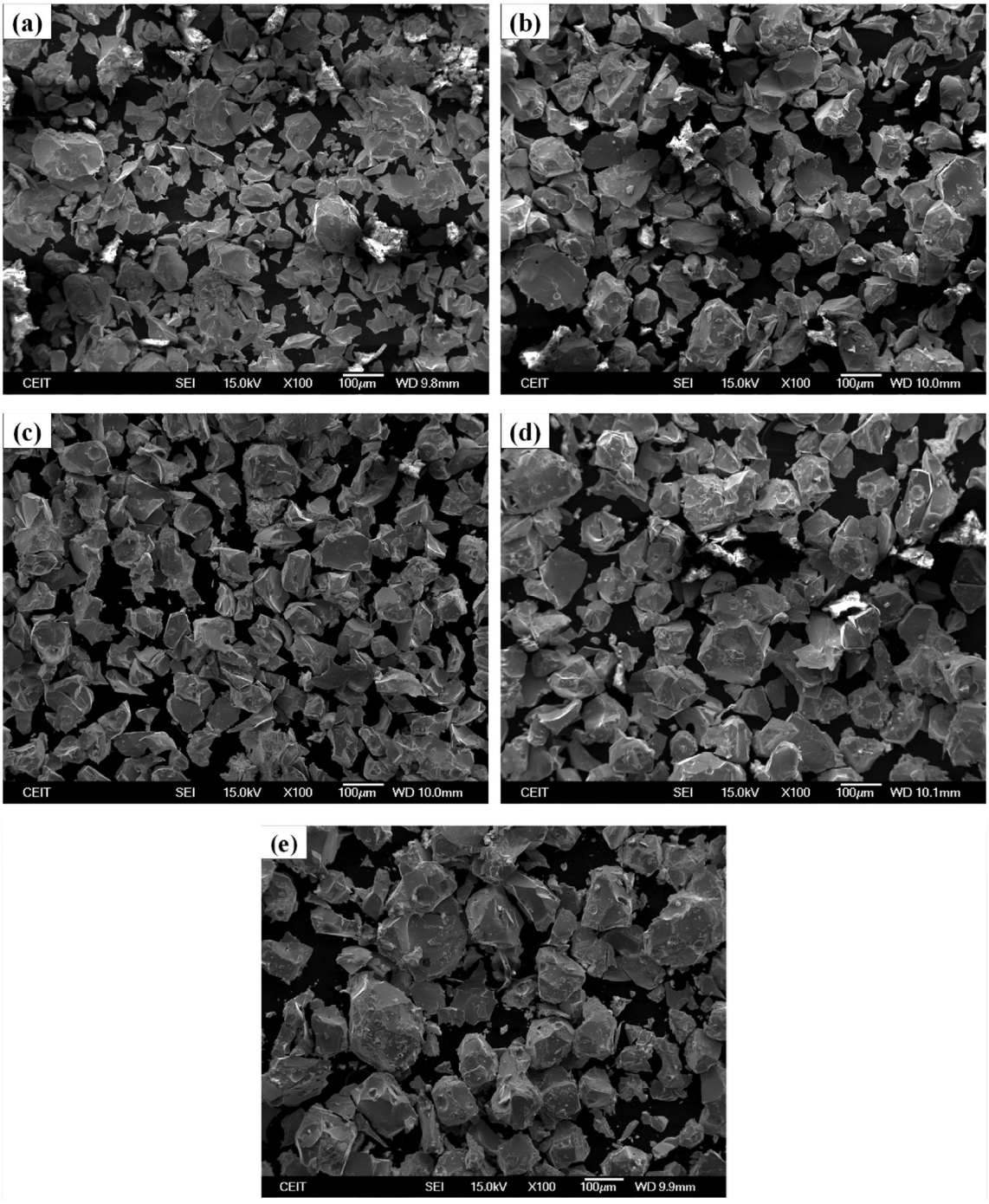


**Fig. 8 – Powder obtained after HD at different temperatures: (a) 25, (b) 50, (c) 100, (d) 150, and (e) 300 °C.**

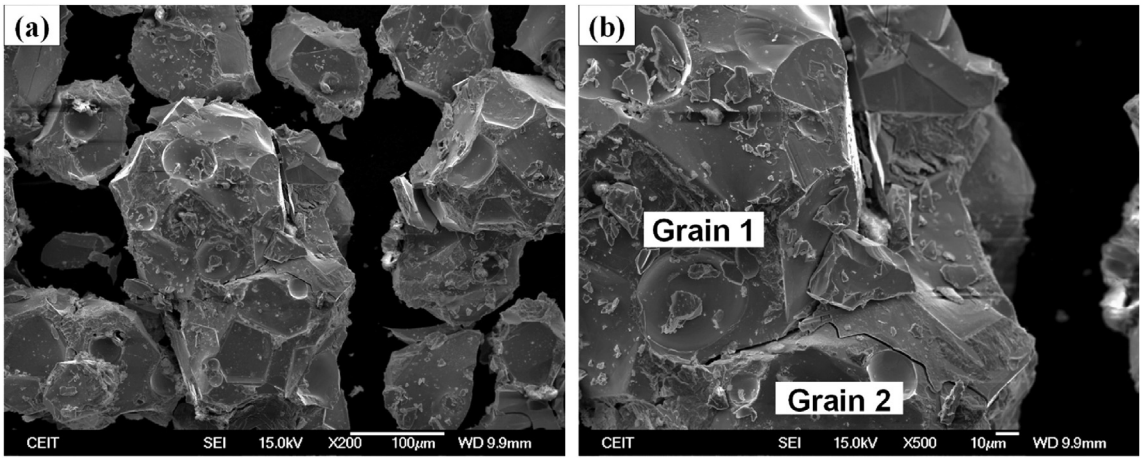


**Fig. 9 – Polycrystalline particles obtained after HD at 300 °C: (a) low magnification and (b) high magnification.**

These qualitative observations have been confirmed with quantitative measurements. Fig. 10 displays the particle size distributions of the different HD powders. Table 4 compares the 10th percentile ($D_{10}$), the median particle size ($D_{50}$), and the 90th percentile ($D_{90}$) of the particle size distributions of the HD powders with those of the grain size distribution of the annealed block. The microstructural values of the annealed block have actually been obtained from a polished cross-section, while those obtained by dynamic image analysis from the HD powders are measured on projected sections. Both cannot be directly compared, since the latter are systematically larger. As explained in Appendix A, the mean cross-sectioned equivalent diameter ($\overline{d_{sec}}$) has to be transformed into a projected equivalent diameter ($\overline{D}$) using the equation $\overline{D} = \frac{4}{\pi}\overline{d_{sec}}$. In the case of the grain size, two set of values are reported in Table 4. The data labeled as "annealed" are the actual measurements. Those data labeled as "corrected annealed" are the actual measurements transformed with the conversion factor "4/π" to be comparable with the projected diameters of HD powders.

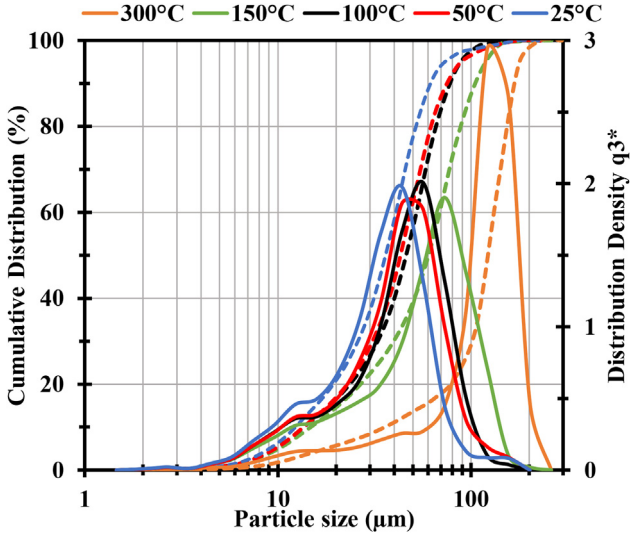


**Fig. 10 – Particle size distribution of HD powders.**

The numbers confirm that the particle size of the HD powder increases with the decrepitation temperature, rising $D_{50}$ from 36.1 up to 122.5 μm. The initial grain size distribution has $D_{50}$ and $D_{90}$ values that lay between those of the HD powder obtained at 150 °C and 300 °C. $D_{10}$ value is lower for all the HD powders than for the original grain size distribution, indicating that transgranular cracking takes place to some extent for all the temperatures, being less pronounced when the temperature is raised. At 300 °C, $D_{50}$ and $D_{90}$ are higher than in the initial annealed block (122.5 versus 88.0 μm for $D_{50}$ and 171.1 versus 147.0 μm for $D_{90}$), verifying the presence of polycrystalline particles. $D_{10}$ should be higher as well, but the contribution of transgranular cracking has maintained constant this parameter in ~35 μm.

The particle shape has been quantitatively evaluated using the aspect ratio of the particles. Fig. 11a shows the aspect ratio versus the particle size for the decrepitated powders at different temperatures. It is noticeable that the aspect ratio rises from less than 0.5 up to 0.9 for all the different hydrogenated powders when the particle size is increased. As the smallest particles have been formed by transgranular

**Table 4 – Comparison of the grain size distribution of the annealed material with the particle size distributions of HD powders.**

| Specimen | Grain/particle size distribution | | |
|---|---|---|---|
| | $D_{10}$ (μm) | $D_{50}$ (μm) | $D_{90}$ (μm) |
| Annealed | 34.6 | 69.1 | 115.4 |
| Corrected annealed | 44.0 | 88.0 | 147.0 |
| HD 25°C | 12.3 | 36.1 | 62.6 |
| HD 50°C | 13.6 | 43.2 | 77.3 |
| HD 100°C | 13.7 | 46.2 | 79.3 |
| HD 150°C | 14.9 | 60.1 | 105.7 |
| HD 300°C | 36.0 | 122.5 | 171.1 |

$D_{10}$: 10th percentile; $D_{50}$: median particle size; $D_{90}$: 90th percentile.

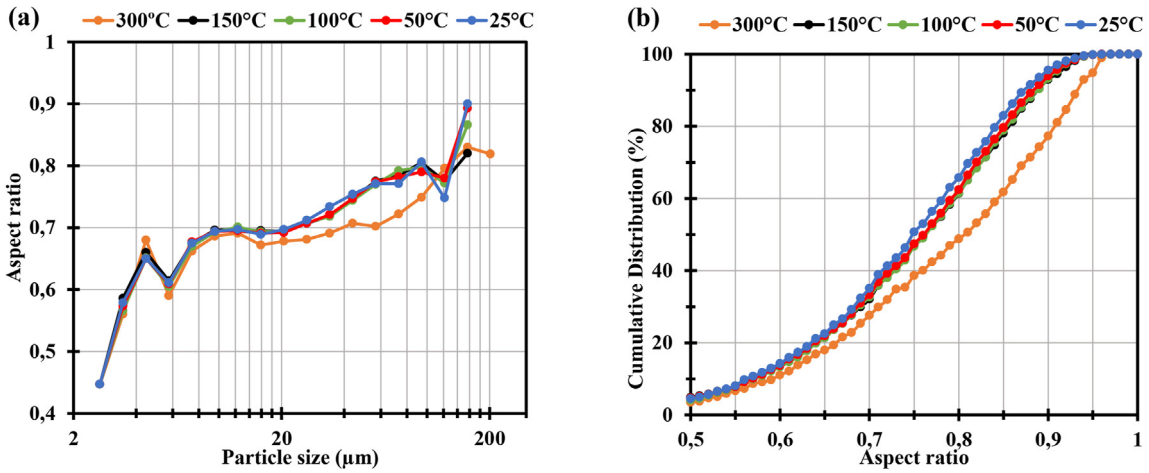


**Fig. 11 – (a) Aspect ratio vs particle size and (b) cumulative distribution of aspect ratio of HD powders decrepitated at different temperatures.**

cracking, they have a more irregular shape. More strikingly, except for the powder decrepitated at 300 °C, the particle shape depends only of the particle size, independently of the decrepitation conditions. In other words, the dominant fracture mechanism is the same. In the case of the sample decrepitated at 300 °C, the behavior is equivalent for particles under 12 μm. Above this size, the particles are clearly more irregular, indicating perhaps the onset of the formation of polycrystalline particles.

Regarding Fig. 11b, we can observe that the aspect ratio distributions move to the right with the rise of the hydrogenation temperature, being this displacement more remarkable when the decrepitation temperature is 300 °C. Thus, any considered percentile ($D_{10}$, $D_{50}$ or $D_{90}$) and the average value of

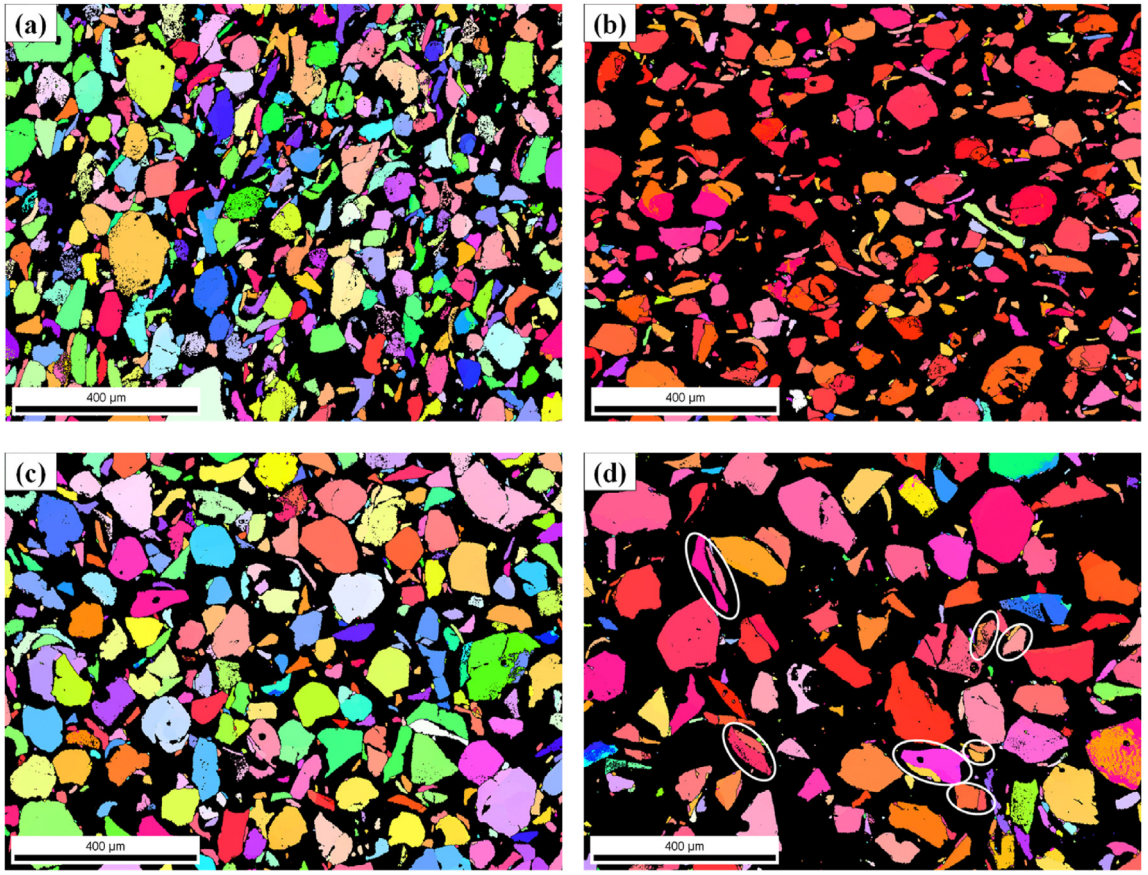


**Fig. 12 – Inverse pole figures (IPF) of HD powders decrepitated at (a) 25, (b) 50, (c) 150, and (d) 300 °C.**

the aspect ratio are always higher when the decrepitation temperature is increased, so that the resulting powder is less irregular. This trend is the expected one, since the irregularity decreases when the particle size increases, i.e. with the decrepitation temperature. The overall irregularity of the powder is determined by the particle size distribution. As explained above, for a given particle size, the polycrystalline particles produced at 300 °C are more irregular, but the overall trend for this powder is as well that the irregularity of the particles decreases when the particle size increases. Compared with the other samples, the powder decrepitated at 300 °C has a higher fraction of large particles, Notice, for example, that more than half of the particles in this sample are larger than 100 μm, according to Fig. 10. Thus, the overall result is that this powder is the less irregular.

IPF figures have been used to evaluate the monocrystalline character of the produced HD powders. Fig. 12 shows the IPF figures of the HD powders decrepitated at different temperatures. It has been confirmed that most of the obtained particles are monocrystalline for any given temperature. Particles are mostly of a single color, showing that they contain a single crystallographic orientation. The pictures show the polished cross-section of the particles. In agreement with Fig. 8, which shows the 3D shape of the same powders using secondary electrons, it is observed that the particle size increases and the particle irregularity decreases when the decrepitation temperature is raised. Some polycrystalline particles are encircled in Fig. 12d, the case of the sample decrepitated at 300 °C. Proportionally, the number of polycrystalline particles in this sample is higher than in the others. Notice that this IPF image contains significantly less particles than the others, as the particle size is larger.

## 4. Conclusions

This work presents a study of the hydrogen decrepitation of a ternary alloy 31.5Nd-bal.Fe-1.1B (wt.%). The following conclusions have been drawn from the obtained results.

a) DSC curves have shown that the kinetics of hydrogen decrepitation accelerates and the released heat rises when the temperature is raised.
b) TGA measurements have demonstrated that hydrogen absorption decreases with the temperature, producing a lower volume expansion.
c) Lattice parameter measurements have revealed that the hydrogen absorbed by the matrix phase decreases with the temperature. It is important to minimize the hydrogenation of the matrix phase during HD to prevent transgranular cracking and the formation of microcracks.
d) A temperature-hydrogen pressure phase diagram is presented that shows the minimum partial pressure of hydrogen at each temperature required to form $Nd_2Fe_{14}BH_y$ and $NdH_{2.7}$ for a 31.5Nd-bal.Fe-1.1B (wt.%) ternary alloy.
e) Particle size and aspect ratio distributions were measured by dynamic image analysis for the powders decrepitated at different temperatures. When the temperature is raised, transgranular breakage is reduced, resulting in a larger particle size and a more equiaxial particle shape, which is important for the subsequent processing of the powder to produce bonded magnets. The overall irregularity of the powder is determined by the particle size distribution.
f) The particle shape and fracture mode depend on the particle size, but not on the decrepitation conditions. The only exception is in the case of particles larger than 12 μm decrepitated at 300 °C, which are clearly more irregular, probably because they are polycrystalline.
g) IPF figures of the HD powders decrepitated at different temperatures confirmed that most of the obtained particles are monocrystalline for any given temperature.
h) It has been determined that the optimum temperature range of hydrogen decrepitation for the subsequent application of the HDDR process is comprised between 150 and 300 °C for a 31.5Nd-balFe-1.1B (wt.%) ternary alloy. As shown schematically in Fig. 1, the degree of transgranular cracking decreases with the temperature, which produces larger particles with an improved shape. At 300 °C, insufficient intergranular fracture results in polycrystalline particles because of the short reaction time (Fig. 1c). The presence of polycrystalline particles will reduce the anisotropy of the final HDDR powder. The best compromise between a high aspect ratio and a low number of polycrystalline particles is obtained between 150 and 300 °C.

## Data availability

The raw/processed data required to reproduce these findings cannot be shared at this time as the data also forms part of an ongoing study.

## Credit authorship contribution statement

**B.L. Checa Fernández:** Formal analysis, Investigation, Methodology, Validation, Visualization, Writing - original draft. **J.M. Martín:** Conceptualization, Funding acquisition, Methodology, Supervision, Writing - review & editing. **G. Sarriegui:** Formal analysis, Writing - review & editing. **N. Burgos:** Formal analysis, Writing review & editing, Supervision.

## Declaration of competing interest

The authors declare that they have no known competing financial interests or personal relationships that could have appeared to influence the work reported in this paper.

## Acknowledgments

This work has received funding from the European Union's Horizon 2020 research and innovation program under grant agreement No 720838 (NEOHIRE project), from the Basque

Country and the European Union through the European Regional Development Fund 2014–2022 (ERDF) (Hazitek 2019 industrial research program Project No ZE-2019/00030 – MADE), and from EIT Manufacturing under program BP2021-22 KAVA 22122 (CheapReMag project).

## Appendix A. Supplementary data

Supplementary data to this article can be found online at https://doi.org/10.1016/j.jmrt.2023.03.076.

## REFERENCES

[1] Croat JJ, Herbst JF, Lee RW, Pinkerton FE. Pr-Fe and Nd-Fe-based materials: a new class of high-performance permanent magnets (invited). J Appl Phys 1984;55:2078–82. https://doi.org/10.1063/1.333571.

[2] Sagawa M, Fujimura S, Togawa N, Yamamoto H, Matsuura Y. New material for permanent magnets on a base of Nd and Fe (invited). J Appl Phys 1984;55:2083–7. https://doi.org/10.1063/1.333572.

[3] Yan G, Williams AJ, Farr JPG, Harris IR. Effect of density on the corrosion of NdFeB magnets. J Alloys Compd 1999;292:266–74. https://doi.org/10.1016/S0925-8388(99)00443-0.

[4] Woodcock TG, Gutfleisch O. Multi-phase EBSD mapping and local texture analysis in NdFeB sintered magnets. Acta Mater 2011;59:1026–36. https://doi.org/10.1016/j.actamat.2010.10.033.

[5] Mo W, Zhang L, Liu Q, Shan A, Wu J, Komuro M. Dependence of the crystal structure of the Nd-rich phase on oxygen content in an Nd-Fe-B sintered magnet. Scripta Mater 2008;59:179–82. https://doi.org/10.1016/j.scriptamat.2008.03.004.

[6] Fidler J. Electron microscopy of Nd-Fe-B based magnets. J Magn Magn Mater 1989;80:48–56.

[7] Makita K, Yamashita O. Phase boundary structure in Nd-Fe-B sintered magnets. Appl Phys Lett 1999;74:2056–8. https://doi.org/10.1063/1.123755.

[8] Hrkac G, Woodcock TG, Butler KT, Saharan L, Bryan MT, Schrefl T, et al. Impact of different Nd-rich crystal-phases on the coercivity of Nd-Fe-B grain ensembles. Scripta Mater 2014;70:35–8. https://doi.org/10.1016/j.scriptamat.2013.08.029.

[9] Yamamoto M, Inoue A, Masumoto T. Production of Nd-Fe-B alloy powders using high-pressure gas atomization and their hard magnetic properties. Metall Trans A 1989;20:5–11. https://doi.org/10.1007/BF02647488.

[10] Sarriegui G, Martin JM, Ipatov M, Zhukov AP, Gonzalez J. Magnetic properties of NdFeB alloys obtained by gas atomization technique. IEEE Trans Magn 2018;54. https://doi.org/10.1109/TMAG.2018.2839906.

[11] Sarriegui G, Martín JM, Burgos N, Ipatov M, Zhukov AP, Gonzalez J. Effect of neodymium content and niobium addition on grain growth of Nd-Fe-B powders produced by gas atomization. Mater Char 2021;172:110844. https://doi.org/10.1016/j.matchar.2020.110844.

[12] Gang Li X, Zhu Q, Shu S, Zhong Fan J, Ming Zhang S. Fine spherical powder production during gas atomization of pressurized melts through melt nozzles with a small inner diameter. Powder Technol 2019;356:759–68. https://doi.org/10.1016/j.powtec.2019.09.023.

[13] Thompson JS, Hassan O, Rolland SA, Sienz J. LSN Diffusion Ltd, the identification of an accurate simulation approach to predict the effect of operational parameters on the particle size distribution (PSD) of powders produced by an industrial close-coupled gas atomiser. Powder Technol 2016;291:75–85. https://doi.org/10.1016/j.powtec.2015.12.001.

[14] Planche MP, Khatim O, Dembinski L, Coddet C, Girardot L, Bailly Y. Velocities of copper droplets in the De Laval atomization process. Powder Technol 2012;229:191–8. https://doi.org/10.1016/j.powtec.2012.06.031.

[15] Ni G, Wang S, Li Q, Zhao D, Song C, Li C. Preparation of Cr17Mn11Mo3N powders by high-pressure gas atomization and the nitrogen increasing mechanism. Powder Technol 2021;385:490–500. https://doi.org/10.1016/j.powtec.2021.03.025.

[16] Zhao Y, Cui Y, Hasebe Y, Bian H, Yamanaka K, Aoyagi K, et al. Controlling factors determining flowability of powders for additive manufacturing: a combined experimental and simulation study. Powder Technol 2021;393:482–93. https://doi.org/10.1016/j.powtec.2021.08.006.

[17] Xiu H, Ma F, Li J, Zhao X, Liu L, Feng P, et al. Using fractal dimension and shape factors to characterize the microcrystalline cellulose (MCC) particle morphology and powder flowability. Powder Technol 2020;364:241–50. https://doi.org/10.1016/j.powtec.2020.01.045.

[18] Gutfleisch O, Harris IR. Fundamental and practical aspects of the hydrogenation, disproportionation, desorption and recombination process. J Phys D Appl Phys 1996;29:2255–65. https://doi.org/10.1088/0022-3727/29/9/006.

[19] Uehara M, Tomizawa H, Hirosawa S, Tomida T, Maehara Y. Origin of anisotropy in the HDDR process of Nd/sub 2/Fe/sub 14/B-based alloys. IEEE Trans Magn 1993;29:2770–2. https://doi.org/10.1109/20.281023.

[20] Tomida T, Choi P, Maehara Y, Uehara M, Tomizawa H, Hirosawa S. Origin of magnetic anisotropy formation in the HDDR-process of Nd2Fe14B-based alloys. J Alloys Compd 1996;242:129–35. https://doi.org/10.1016/0925-8388(96)02378-X.

[21] Sepehri-Amin H, Ohkubo T, Hono K, Güth K, Gutfleisch O. Mechanism of the texture development in hydrogen-disproportionation-desorption-recombination (HDDR) processed Nd-Fe-B powders. Acta Mater 2015;85:42–52. https://doi.org/10.1016/j.actamat.2014.11.003.

[22] Yang Y, Walton A, Sheridan R, Güth K, Gauß R, Gutfleisch O, et al. REE recovery from end-of-life NdFeB permanent magnet scrap: a critical review. J. Sustain. Metall. 2017;3:122–49. https://doi.org/10.1007/s40831-016-0090-4.

[23] Lixandru A, Poenaru I, Güth K, Gauß R, Gutfleisch O. A systematic study of HDDR processing conditions for the recycling of end-of-life Nd-Fe-B magnets. J Alloys Compd 2017;724:51–61. https://doi.org/10.1016/j.jallcom.2017.06.319.

[24] Durrant AJ. The effect of microstructure and composition on HDDR processing of scrap magnets. 2013. p. 105.

[25] Mishima C, Hamada N, Mitarai H, Honkura Y. Development of a Co-free NdFeB anisotropic bonded magnet produced from the d-HDDR processed powder. IEEE Trans Magn 2001;37:2467–70. https://doi.org/10.1109/20.951205.

[26] Harris IR, Evans JM, Nyholm PS. Rare earth metal alloy magnets. Patent 1979;vol. 155.

[27] Harris IR, Noble C, Bailey T. The hydrogen decrepitation of an Ndi15Fe77B8 magnetic alloy. J Less Common Met 1985;106. https://doi.org/10.1016/0022-5088(85)90380-7.

[28] Ragg OM, Keegan G, Nagel H, Harris IR. The HD and HDDR processes in the production of Nd-Fe-B permanent magnets. Int J Hydrogen Energy 1997;22:333–42. https://doi.org/10.1016/s0360-3199(96)00174-7.

[29] Piotrowicz A, Pietrzyk S, Noga P. Myćka, the use of thermal hydrogen decrepitation to recycle Nd-Fe-B magnets from

electronic waste. J Min Metall B Metall 2021;57:297. https://doi.org/10.2298/JMMB2102297E. 297.
[30] Michalski B, Szymanski M, Gola K, Zygmuntowicz J, Leonowicz M. Experimental evidence for the suitability of the hydrogen decomposition process for the recycling of Nd-Fe-B sintered magnets. J Magn Magn Mater 2022;548. https://doi.org/10.1016/j.jmmm.2021.168979.
[31] Isnard O, Yelon WB, Miraglia S, Fruchart D. Neutron-diffraction study of the insertion scheme of hydrogen in Nd 2Fe14B. J Appl Phys 1995;78:1892–8. https://doi.org/10.1063/1.360720.
[32] Harris IR, McGuiness PJ. Hydrogen: its use in the processing of NdFeB-type magnets. J Less Common Met 1991;172–174:1273–84. https://doi.org/10.1016/S0022-5088(06)80037-8.
[33] Horikawa T, Yamazaki M, Matsuura M, Sugimoto S. Recent progress in the development of high-performance bonded magnets using rare earth–Fe compounds. Sci Technol Adv Mater 2021;22:729–47. https://doi.org/10.1080/14686996.2021.1944780.
[34] Schlapbach L, Anderson I, Laue-langevin I, Burger JP. Hydrogen in metals. Mater Sci Technol 2006;12:272–326.
[35] Liszkowski P, Turek K, Figiel H. The influence of decrepitation on the diffusion kinetics of hydrogen in Nd–Fe–B. J Alloys Compd 2000;307:297–303.
[36] Urionabarrenetxea E, Martín JM, Avello A, Rivas A. Simulation and validation of the gas flow in close-coupled gas atomisation process: influence of the inlet gas pressure and the throat width of the supersonic gas nozzle. Powder Technol 2022;407. https://doi.org/10.1016/j.powtec.2022.117688.
[37] Zhang LC, Xu WY, Li Z, Zheng L, Liu YF, Zhang GQ. Characterization of particle shape of nickel-based superalloy powders using image processing techniques. Powder Technol 2022;395:787–801. https://doi.org/10.1016/j.powtec.2021.10.013.
[38] Goto R, Sugimoto S, Matsuura M, Tezuka N, Une Y, Sagawa M. Nd-Fe-B sintered magnets fabrication by using atomized powders. J. Phys. Conf. Ser. 2011;266. https://doi.org/10.1088/1742-6596/266/1/012029.
[39] Gao MZ, Ludwig B, Palmer TA. Impact of atomization gas on characteristics of austenitic stainless steel powder feedstocks for additive manufacturing. Powder Technol 2021;383:30–42. https://doi.org/10.1016/j.powtec.2020.12.005.
[40] Zakotnik M, Harris IR, Williams AJ. Possible methods of recycling NdFeB-type sintered magnets using the HD/degassing process. J Alloys Compd 2008;450:525–31. https://doi.org/10.1016/j.jallcom.2007.01.134.
[41] Yartys VA, Gutfleisch O, Harris IR. Hydrogen-induced phase and magnetic transformations in Nd1.1Fe4B4. J Magn Magn Mater 1996;157–158:119–20. https://doi.org/10.1016/0304-8853(95)01085-8.
[42] Sasaki TT, Ohkubo T, Hono K. Structure and chemical compositions of the grain boundary phase in Nd-Fe-B sintered magnets. Acta Mater 2016;115:269–77. https://doi.org/10.1016/j.actamat.2016.05.035.
[43] Williams AJ, McGuiness PJ, Harris IR. Mass spectrometer hydrogen desorption studies on some hydrided NdFeB-type alloys. J Less Common Met 1991;171:149–55. https://doi.org/10.1016/0022-5088(91)90271-5.
[44] Choi M, Cho S, Jo I, Song Y, Kim C, Yu J, et al. Boron behavior induced lamellar structure and anisotropic magnetic properties of Nd2Fe14B during HDDR process. J Kor Phys Soc 2017;71:130–3. https://doi.org/10.3938/jkps.71.130.
[45] Brooks O, Walton A, Zhou W, Harris IR. The hydrogen ductilisation process (HyDP) for shaping NdFeB magnets. J Alloys Compd 2017;703:538–47. https://doi.org/10.1016/j.jallcom.2016.12.177.
[46] Bezdushnyi R, Damianova R, Tereshina IS, Pankratov NY, Nikitin SA. Hydrogen absorption and its effect on magnetic properties of Nd 2 Fe 14 B. J Magn Magn Mater 2018;453:226–30. https://doi.org/10.1016/j.jmmm.2017.12.102.